QUANTUM SIMULATION

Coherent imaging spectroscopy of a quantum many-body spin system

C. Senko,[1]* J. Smith,[1] P. Richerme,[1] A. Lee,[1] W. C. Campbell,[2] C. Monroe[1]

Quantum simulators, in which well-controlled quantum systems are used to reproduce the dynamics of less understood ones, have the potential to explore physics inaccessible to modeling with classical computers. However, checking the results of such simulations also becomes classically intractable as system sizes increase. Here, we introduce and implement a coherent imaging spectroscopic technique, akin to magnetic resonance imaging, to validate a quantum simulation. We use this method to determine the energy levels and interaction strengths of a fully connected quantum many-body system. Additionally, we directly measure the critical energy gap near a quantum phase transition. We expect this general technique to become a verification tool for quantum simulators once experiments advance beyond proof-of-principle demonstrations and exceed the resources of conventional computers.

Certain classes of quantum many-body systems, including high-temperature superconductors and spin liquids, are believed to be fundamentally inaccessible to classical modeling (1). For example, interacting spin systems described by the Ising model can be mapped to NP-complete computational problems (2) and have been applied to understanding neural networks (3) and social behavior (4), yet quickly become theoretically intractable because of the exponential number of possible spin configurations (5).

Quantum simulations (6–8), in which well-controlled quantum objects like photons (9) or ultracold atoms (10, 11) are induced to emulate other quantum systems, are a promising alternative for accessing such problems. However, as these systems approach theoretically intractable physics, validating quantum simulation results will become a major challenge (1, 12). Here, we introduce a technique for performing coherent imaging spectroscopy on the Hamiltonian of an interacting many-body spin system. We use spectroscopic imaging to infer spin-spin interaction strengths and directly measure the critical energy gap near a quantum phase transition.

Ultracold atomic systems are particularly well suited for simulating interacting spin systems, with the ability to prepare known input states, engineer tunable interaction patterns, and measure individual particles (10, 11). Our experiment uses trapped ions to simulate chains of spin-1/2 particles subject to effective magnetic fields and long-range, inhomogenous Ising couplings generated by optical dipole forces (13–19). This results in an effective N-spin Hamiltonian (with the Planck constant $h = 1$)

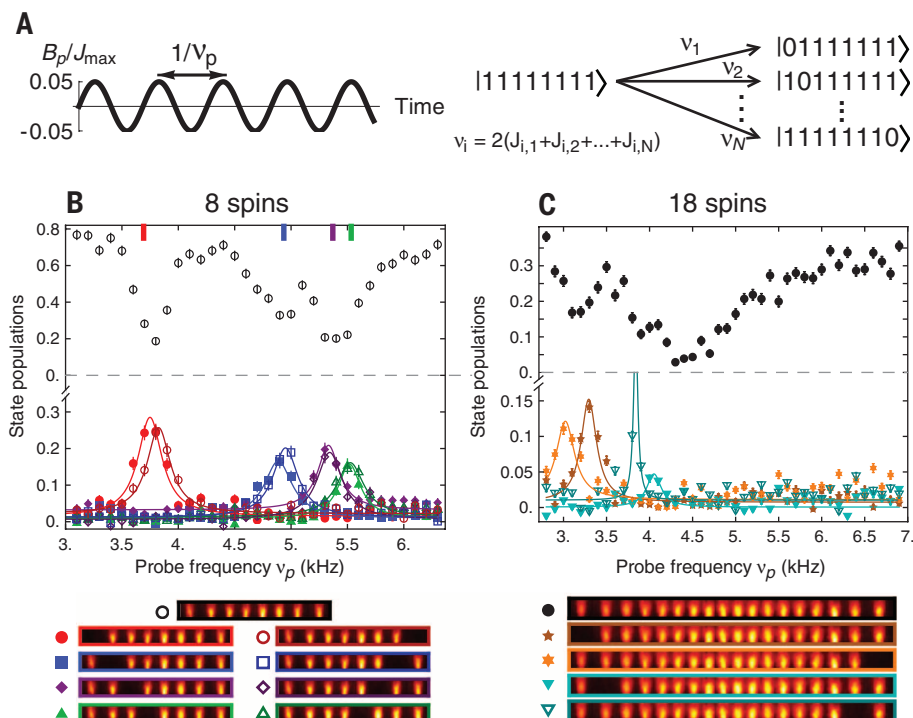$$H_{\text{eff}} = \sum_{i<j} J_{i,j}\sigma_i^x\sigma_j^x + B(t)\sum_i \sigma_i^y, \qquad (1)$$

where σ_i^γ ($\gamma = x, y, z$) is the Pauli matrix for spin i along direction γ; $J_{i,j} \sim J_0|i-j|^{-\alpha}$ is a long-range coupling strength between spins i and j with $J_0 > 0$ and α tunable between 0 and 3 (13); and $B(t)$ is the energy associated with a time-dependent transverse magnetic field (20).

The ability to generate antiferromagnetic $J_{i,j}$ couplings of varying interaction range (13, 17, 18) has recently attracted much interest in contexts such as studying the spread of correlations after a quench (21, 22), observing prethermalization of a quantum system (23, 24), and directly measuring response functions (25). Developing a general protocol to measure the spin-spin couplings will be an important validation goal. Previous experiments have fully characterized the interactions in small systems using techniques that may be difficult to scale up, such as Fourier decomposition of multispin dynamics (14) or manipulating each of the ~$N^2/2$ pairs of spins separately using electromagnetic field gradients for frequency (26) or spatial addressing (27). By contrast, the protocol we introduce below allows the couplings

[1]Joint Quantum Institute, University of Maryland, Department of Physics, and National Institute of Standards and Technology, College Park, MD 20742, USA. [2]Department of Physics and Astronomy, University of California, Los Angeles, CA 90095, USA.
*Corresponding author. E-mail: csenko@umd.edu

Fig. 1. Principle of coherent imaging spectroscopy. (**A**) The transverse field term B_p drives transitions between states when its modulation frequency matches an allowed energy splitting (such as between the state with all spins up along x and any single-defect state with a single spin down). (**B**) Measured populations in specific spin states (see legend, bottom, where a fluorescing (dark) ion represents $|1\rangle$ [$|0\rangle$)]) versus the frequency of the probe field for a system of eight spins initialized in $|11111111\rangle$ before probing. Solid curves are Lorentzians fit to the data sets; the energy splittings predicted from Eq. 1 are indicated with colored bars at the top of the frame. Error bars represent statistical error from performing 1000 repetitions of each experiment. (**C**) Measured populations versus the frequency of the probe field for a system of 18 spins. The left-right asymmetry is attributed to slight misalignment of the laser beams. Despite the low fidelity of the initial state (35% in the $|111111111111111111\rangle$ state), these energy splittings are still clearly visible.

to be measured by taking ~N frequency spectra and requires only global interactions and site-resolved measurements.

The spin-1/2 particles are represented by a string of ^{171}Yb$^+$ ions confined in a linear Paul trap. The spin states $|\downarrow\rangle_z$ and $|\uparrow\rangle_z$ are encoded in the magnetic-field-insensitive ($m_F = 0$) hyperfine states of the ground electronic manifold (28). The spin-spin couplings and effective magnetic fields derive from lasers that globally illuminate the ion chain, driving stimulated Raman transitions between the spin states (14, 20). State initialization comprises optical pumping into the $|\downarrow\downarrow\downarrow\cdots\rangle_z$ state followed by a coherent rotation to polarize all spins along the desired axis. After applying the spin-spin couplings and the probe field(s) described above, the individual spin states are read out along any axis by performing a coherent rotation from that axis to the measurement basis $|\downarrow\rangle_z$ and $|\uparrow\rangle_z$, then collecting state-dependent fluorescence onto a charge-coupled device imager with site-resolving optics (20).

We measure the energy splittings in our spin system using a weakly modulated transverse field as a probe.

$$B(t) = B_0 + B_p \sin(2\pi\nu_p t) \qquad (2)$$

When the probe frequency ν_p is matched to the energy difference $|E_a - E_b|$ between two eigenstates $|a\rangle$ and $|b\rangle$, the field will drive transitions between the two states if there is a nonzero matrix element $\langle b|B(t)\sum_i \sigma_i^y|a\rangle \neq 0$. For example, in the weak-field regime $B(t) << J_0$, the Hamiltonian eigenstates are symmetric combinations of the σ^x eigenstates, and the matrix element $\langle b|B(t)\sum_i \sigma_i^y|a\rangle$ is nonzero only when $|a\rangle$ and $|b\rangle$ differ by the orientation of exactly one spin.

In the weak-field regime, a transition at a single frequency can easily be monitored, and its stability can provide a good proxy for the entire Hamiltonian. Each splitting depends on multiple spin-spin couplings—for example, a transition from $|1111\cdots\rangle$ to $|0111\cdots\rangle$, where $|1\rangle$ ($|0\rangle$) denotes the σ^x eigenstate $|\uparrow\rangle_x$ ($|\downarrow\rangle_x$), requires energy

$$\Delta E = 2(J_{1,2} + J_{1,3} + \cdots + J_{1,N}) \qquad (3)$$

These splittings are therefore sensitive to changes in the motional mode structure or the laser intensities at each of the ions.

We demonstrate the mapping of individual energy splittings in the weak-field regime $B(t)/J_0 << 1$ in Fig. 1. The spins are prepared along the x direction in $|111\cdots\rangle$, and a probe field corresponding to $B(t) = (100 \text{ Hz})\sin(2\pi\nu_p t)$ is applied for 3 ms, which is sufficient to transfer more than 50% of the population between states, before measuring along x. These parameters allow resolution of the energy differences in an eight-spin system while still accommodating the few ms decoherence time scale in our system (18).

Population transfer is clearly seen when ν_p is resonant with an energy splitting (e.g., Fig. 1, B and C). We quantify the energy of a particular state relative to the initial state by fitting Lorentzians to the spectra (20). The spectral positions are insensitive to state preparation and measurement error, which affects only the contrast of these resonances, as seen in Fig. 1C with $N = 18$ spins.

A sequence of multiple probe frequencies (shown in fig. S1) can be used to populate any desired spin configuration with a global beam in no more than $\lfloor N/2 \rfloor$ pulses. We can transfer population into any of the 32 eigenstates of a five-spin system by starting in either the $|11111\rangle$ or $|00000\rangle$ and applying at most two pulses of the transverse field. This system is small enough to also measure the entire relative energy spectrum, which scales exponentially with system size. Starting from the states $|11111\rangle$, $|00000\rangle$, $|10101\rangle$, and $|01010\rangle$ [the last two of which are prepared using an adiabatic ramp of a transverse field (18)], we use single and multiple frequency drives to measure all possible energy splittings.

Figure 2 shows the measured spectrum of this five-spin system, obtained by direct addition of the measured energy splittings, compared to that given by the interactions estimated from the same data (as detailed below). An examination of the full spectrum of a many-body quantum system is generally difficult to achieve and shows the versatility of this form of many-body spectroscopy.

We can also use modulated transverse fields to prepare arbitrary coherent quantum states, which can be used to probe many-body quantum dynamics (24). An example protocol for preparing a specific spin configuration is shown in fig. S1.
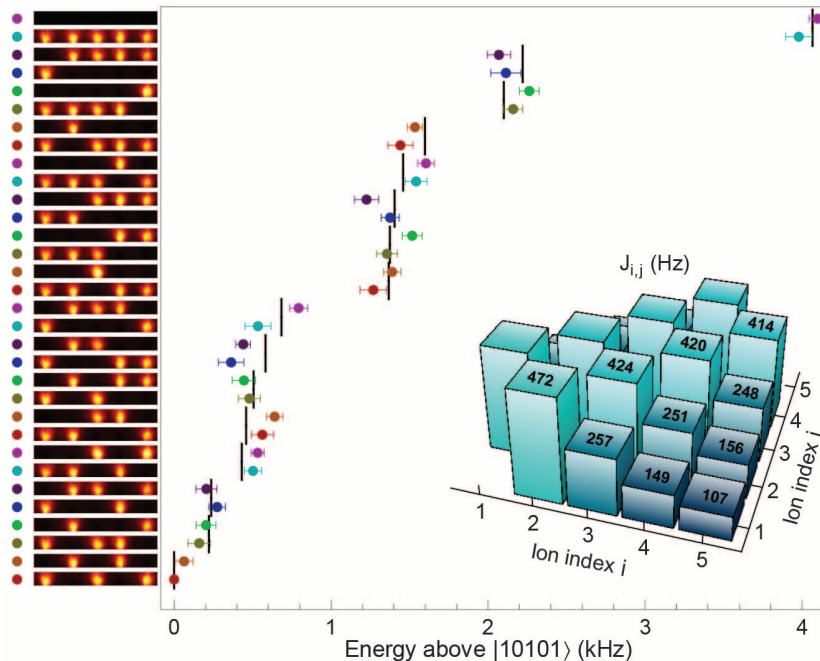

Fig. 2. Reconstructed energy spectrum. In a system of five spins, the energy of each spin configuration above the $|10101\rangle$ ground state (colored points) is compared to the calculated energies (black lines). Calculations are based on the spin-spin couplings estimated from the same energy measurements (inset). Error bars include statistical errors and an estimate of systematic error due to experimental drifts.
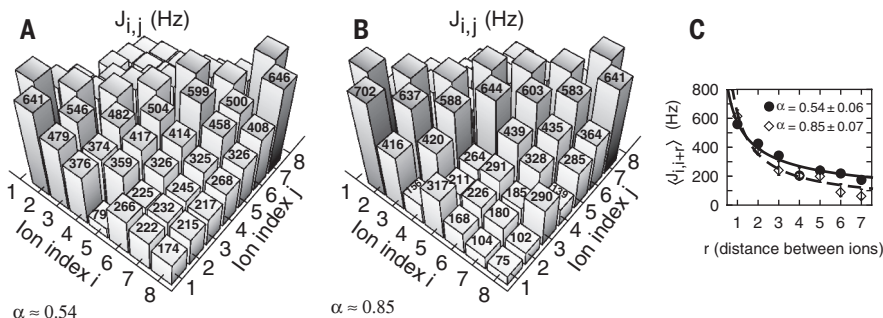

Fig. 3. Experimentally determined spin-spin coupling profiles. The couplings were measured in a system of eight spins for two sets of trap parameters, corresponding to a more long-range or more short-range interaction profile. (**A**) and (**B**) depict the individual elements of the measured coupling matrix. (**C**) plots measured average interactions against ion separation and shows fits to a power law J_0/r^α. The error in α is an estimate of the standard error in the fit parameter; this takes into account the errors in the $J_{i,j}$ estimates based on fit error and statistical error in population measurements (20).

In general, subjecting a left-right symmetric state to a global resonant probe field prepares symmetric superpositions of states that exhibit a degree of entanglement, although this is difficult to detect without individual rotations for readout.

We generate entanglement by subjecting an initial state $|111\cdots11\rangle$ to multiple frequencies simultaneously, such that all of the possible transitions are driven equally. After an appropriate time, the system will ideally be driven into a W-type state of the form

$$|\Psi_W\rangle = \frac{1}{\sqrt{N}}\Big(e^{i\phi_0}|011\cdots11\rangle + e^{i\phi_1}|101\cdots11\rangle +$$
$$\cdots + e^{i\phi_1}|111\cdots01\rangle + e^{i\phi_0}|111\cdots10\rangle\Big) \quad (4)$$

where the phases ϕ_i depend on the relative phase of the applied modulation frequencies. Entanglement can then be detected using global measurements of the magnetization along various directions of the Bloch sphere (29). In particular, we use a witness operator

$$W_{ss} = (N-1)(<J_x^2> - <J_x>^2) + \frac{N}{2} -$$
$$<J_y^2> - <J_z^2> \quad (5)$$

where $J_\gamma \equiv \frac{1}{2}\sum_{i=1}^{N}\sigma_i^\gamma$ (with appropriate phases) and angle brackets denote ensemble averages. This spin-squeezing observable will always be positive for separable states, so measurement of a negative value certifies that at least two particles are entangled. We prepare an entangled state of four spins by applying two simultaneous frequencies of the modulated transverse field to the state $|1111\rangle$ with an appropriate relative phase for

1.8 ms and measure the resulting state along the Bloch sphere directions x, y, and z to obtain the witness shown above. This certifies that the full state is entangled. Moreover, individual spin-state imaging allows us to trace over any given spin or pair of spins and apply the witness to this reduced density matrix. Table S1 displays these data, which is consistent with entanglement in every possible reduced state.

Many-body spectroscopy using a transverse probe field further enables determination of each individual spin-spin coupling $J_{i,j}$. Using only $N + 1$ scans of the probe frequency, we can measure $\binom{N}{2} = N(N-1)/2$ energy splittings and thus determine the entire interaction matrix of $\binom{N}{2}$ couplings (e.g., Eq. 3). For example, one scan probes the state $|1111\cdots\rangle$ and yields the N energy splittings to the single-defect states. Then, as in fig. S1, N additional scans starting from each single-defect state determine $N-1$ further energy splittings. In total, these $N + 1$ scans yield N^2 measurements [N from the first probe scan and $N(N-1)$ from the rest]. Because of the parallel processing enabled by imaging individual spin states, the number of measurements to evaluate all spin-spin couplings scales only linearly with the system size (20). We perform this verification protocol on a system of eight spins with two different interaction ranges. We can measure the full interaction matrix with five frequency scans; because of the left-right symmetry, single-defect states are populated in pairs and only four scans are necessary to probe all eight of the defect states. In contrast, mapping all 2^N energies (as done above with five spins) would already require ~100 scans for an eight-spin system. The obtained matrix

agrees well with theory; roughly 70% of measured interactions match the prediction within 1σ standard error. We observe a distinction in the coupling matrices for differently chosen ranges of spin-spin interactions (Fig. 3).

Finally, we probe energy levels at nonzero transverse field B_0, including near the critical region $B_0 \approx <J>$. Determining the critical energy gap Δ, at which the energy difference between the ground and lowest coupled excited states is minimized, is useful because this parameter determines the ability to perform an adiabatic sweep of the transverse field (19, 30). However, measuring the critical gap is difficult in general because of the inability to measure or even know the instantaneous eigenbasis.

The protocol described in Fig. 1 is effective even when there is a small dc field B_0 (Fig. 4, A and B) but breaks down near the critical region. However, for a finite-size ferromagnetic system, measurements along a different axis of the Bloch sphere (here, $\hat{x} + \hat{y}$) allow us to still observe transitions from the ground to the first coupled excited state near the critical gap (Fig. 4, C and D). As shown in Fig. 4E, these experiments allow us to map the lowest coupled excited state from $B_0 = 0$ beyond the critical energy gap Δ. The downward drift in energies near $B_0 = 0$ can be attributed to drifts in laser and trap parameters as the experiments progressed from higher to lower fields. An alternative protocol, which follows the time evolution after a quench, has recently been proposed for measuring the critical gap and may scale better for larger systems (31).

Our technique will no doubt benefit from further refinements borrowing from the extensive literature of spectroscopic methods developed in other fields, such as nuclear magnetic
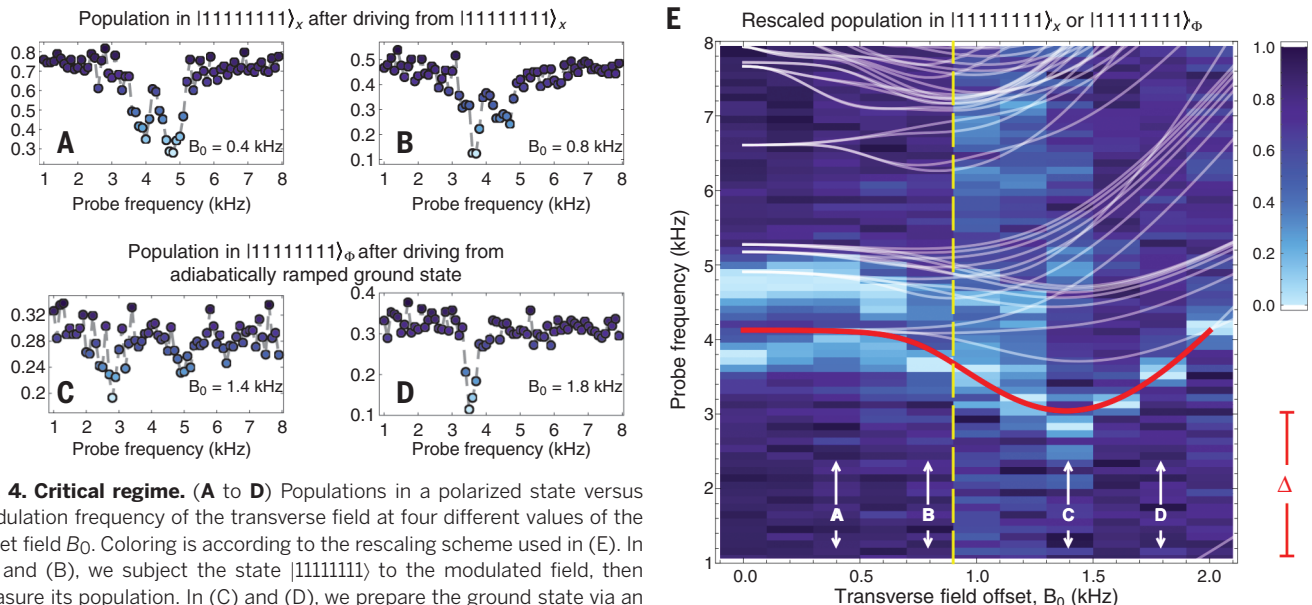

Fig. 4. Critical regime. (**A** to **D**) Populations in a polarized state versus modulation frequency of the transverse field at four different values of the offset field B_0. Coloring is according to the rescaling scheme used in (E). In (A) and (B), we subject the state $|11111111\rangle$ to the modulated field, then measure its population. In (C) and (D), we prepare the ground state via an adiabatic ramp, subject it to the modulated field, and then measure the population in $|\uparrow\uparrow\uparrow\uparrow\uparrow\uparrow\uparrow\uparrow\rangle_\phi$. (**E**) Rescaled populations in $|11111111\rangle$ (left of the dashed line) or $|\uparrow\uparrow\uparrow\uparrow\uparrow\uparrow\uparrow\uparrow\rangle_\phi$ (right of the dashed line) versus static field offset B_0 and modulation frequency. Calculated energy levels, based on measurements of trap and laser parameters, are overlaid as thin white lines, and the lowest coupled excited state as a thick red line, showing the critical gap Δ at position C. The energy of the ground state is always taken to be zero.

resonance (*32*). In addition, the protocol developed here is general and will affect experiments with ion traps and other platforms as system sizes increase, both in full calibrations of the coupling matrix and in the ability to observe a single quantity that serves as a proxy for the entire Hamiltonian.

REFERENCES AND NOTES

1. J. I. Cirac, P. Zoller, *Nat. Phys.* **8**, 264–266 (2012).
2. B. A. Cipra, *SIAM News* **33** (6), 654 (2000); www.siam.org/pdf/news/654.pdf.
3. E. Schneidman, M. J. Berry 2nd, R. Segev, W. Bialek, *Nature* **440**, 1007–1012 (2006).
4. S. Liu, L. Ying, S. Shakkottai, in *48th Annual Allerton Conference on Communication, Control, and Computing* (IEEE, New York, 2010), pp. 570–576.
5. H. T. Diep, Ed., *Frustrated Spin Systems* (World Scientific, Singapore, 2005).
6. R. Feynman, *Int. J. Theor. Phys.* **21**, 467–488 (1982).
7. S. Lloyd, *Science* **273**, 1073–1078 (1996).
8. *Nature Physics*, Insight Issue: "Quantum Simulation" **8**, 264 (2012).
9. A. Aspuru-Guzik, P. Walther, *Nat. Phys.* **8**, 285–291 (2012).
10. R. Blatt, C. F. Roos, *Nat. Phys.* **8**, 277–284 (2012).
11. I. Bloch, J. Dalibard, S. Nascimbene, *Nat. Phys.* **8**, 267–276 (2012).
12. P. Hauke, F. M. Cucchietti, L. Tagliacozzo, I. Deutsch, M. Lewenstein, *Rep. Prog. Phys.* **75**, 082401 (2012).
13. D. Porras, J. I. Cirac, *Phys. Rev. Lett.* **92**, 207901 (2004).
14. K. Kim et al., *Phys. Rev. Lett.* **103**, 120502 (2009).
15. K. Kim et al., *Nature* **465**, 590–593 (2010).
16. R. Islam et al., *Nat. Commun.* **2**, 377 (2011).
17. J. W. Britton et al., *Nature* **484**, 489–492 (2012).
18. R. Islam et al., *Science* **340**, 583–587 (2013).
19. P. Richerme et al., *Phys. Rev. A* **88**, 012334 (2013).
20. Materials and methods are available as supplementary material on *Science* Online.
21. J. Schachenmayer, B. P. Lanyon, C. F. Roos, A. J. Daley, *Phys. Rev. X* **3**, 031015 (2013).
22. P. Hauke, L. Tagliacozzo, *Phys. Rev. Lett.* **111**, 207202 (2013).
23. M. van den Worm, B. C. Sawyer, J. J. Bollinger, M. Kastner, *New J. Phys.* **15**, 083007 (2013).
24. Z.-X. Gong, L.-M. Duan, *New J. Phys.* **15**, 113051 (2013).
25. M. Knap et al., *Phys. Rev. Lett.* **111**, 147205 (2013).
26. A. Khromova et al., *Phys. Rev. Lett.* **108**, 220502 (2012).
27. P. Jurcevic et al., *Nature* **511**, 202–205 (2014).
28. S. Olmschenk et al., *Phys. Rev. A* **76**, 052314 (2007).
29. G. Tóth, C. Knapp, O. Gühne, H. J. Briegel, *Phys. Rev. Lett.* **99**, 250405 (2007).
30. E. E. Edwards et al., *Phys. Rev. B* **82**, 060412 (2010).
31. B. Yoshimura, W. C. Campbell, J. K. Freericks, http://arxiv.org/abs/1402.7357 (2014).
32. R. R. Ernst, G. Bodenhausen, A. Wokaun, *Principles of Nuclear Magnetic Resonance in One and Two Dimensions* (Clarendon Press, Oxford, 1987).

DUAL CATALYSIS

Single-electron transmetalation in organoboron cross-coupling by photoredox/nickel dual catalysis

John C. Tellis,* David N. Primer,* Gary A. Molander†

The routine application of C_{sp3}-hybridized nucleophiles in cross-coupling reactions remains an unsolved challenge in organic chemistry. The sluggish transmetalation rates observed for the preferred organoboron reagents in such transformations are a consequence of the two-electron mechanism underlying the standard catalytic approach. We describe a mechanistically distinct single-electron transfer-based strategy for the activation of organoboron reagents toward transmetalation that exhibits complementary reactivity patterns. Application of an iridium photoredox catalyst in tandem with a nickel catalyst effects the cross-coupling of potassium alkoxyalkyl- and benzyltrifluoroborates with an array of aryl bromides under exceptionally mild conditions (visible light, ambient temperature, no strong base). The transformation has been extended to the asymmetric and stereoconvergent cross-coupling of a secondary benzyltrifluoroborate.

The immense impact of transition metal–catalyzed cross-coupling has been well recognized, with the Suzuki-Miyaura reaction in particular emerging as a preferred method for the construction of C-C bonds in both industrial and academic settings (*1*). Traditionally, cross-coupling reactions employ a three-step catalytic cycle (Fig. 1): (i) oxidative addition of an organic halide at Pd^0, (ii) transmetalation of an organometallic nucleophile to an organopalladium(II) electrophile, and (iii) reductive elimination from a diorganopalladium(II) species, releasing the coupled product and regenerating the Pd^0 catalyst (*1*, *2*). Although these methods are highly effective for C_{sp2}-C_{sp2} coupling, extension to C_{sp3} centers has proven challenging because of lower rates of oxidative addition and transmetalation, as well as the propensity of the alkylmetallic intermediates to undergo facile β-hydride elimination (*2*). Recent advances in ligand technology and the use of alternative metals, such as nickel, have greatly expanded the scope of the electrophilic component, extending even to sterically hindered and unactivated alkyl substrates, and have largely succeeded in retarding problematic β-hydride elimination (*3*). Despite the progress achieved in advancement of the other fundamental steps, transmetalation has remained largely unchanged since the inception of cross-coupling chemistry. As such, cross-couplings conducted under the traditional mechanistic manifold typically result in transmetalations that are rate-limiting (*4*).

To date, strategies aimed at accelerating the rate of transmetalation of C_{sp3}-hybridized boronic acid reagents have been largely rudimentary. In most cases, excess base and high temperature are used, thereby limiting functional group tolerance and augmenting deleterious side reactions (*5*). Stoichiometric Ag and Cu salts have been shown to improve transmetalation efficiency in some systems (*6–8*), although the mechanism by which the acceleration is achieved is unclear (*9*), thus limiting their widespread application. Often, the only viable alternative to overcome a slow transmetalation is to abandon the readily available boronic acids and make use of more reactive organometallic reagents. Thus, alkylboranes, alkylzincs, or the corresponding Grignard reagents—all of which lack functional group tolerance and are unstable to air—are often used for alkyl cross-coupling (*1*).

The challenge of alkylboron transmetalation was recognized to arise directly from mechanistic limitations inherent in the two-electron nature of the conventional process, wherein reactivity is inversely proportional to heterolytic C-B bond strength, thus predisposing C_{sp3} nucleophiles for failure in cross-coupling reactions (*10*, *11*). Rather than attempting to override the inherent biases of the conventional transmetalation pathway, we anticipated that development of an activation mode based on single-electron transfer (SET) chemistry would constitute a more efficient strategy for engaging this class of reagents (Fig. 1). Trends in homolytic C-B bond strength (*12*) dictate that such a reaction manifold would exhibit reactivity trends complementary to that of a traditional cross-coupling, with C_{sp3}-hybridized nucleophiles now ideally primed for successful implementation.

The first challenge associated with the realization of this ideal is the oxidative profile of radical capture at a transition metal center ($R\cdot + M^n \rightarrow R\text{-}M^{n+1}$), which necessitates a subsequent reduction to maintain the redox neutrality of a traditional transmetalation. Here, application of visible-light photoredox catalysis (*13*, *14*), was envisioned to satisfy the requirements of this unique series of SETs. Encouragement in this

Roy and Diana Vagelos Laboratories, Department of Chemistry, University of Pennsylvania, Philadelphia, PA 19104, USA.
*These authors contributed equally to this work. †Corresponding author. E-mail: gmolandr@sas.upenn.edu